

# Triple-energy computed tomography in the megavoltage-range with an inverse Compton scattering light source\*

Zhijun Chi,<sup>1,†</sup> Shengyuan Liu,<sup>1</sup> Hongze Zhang,<sup>2</sup> Jiayi Sun,<sup>2</sup> Hao Ding,<sup>2</sup> Jin Lin,<sup>2</sup> Xuanqi Zhang,<sup>2</sup> Qili Tian,<sup>2</sup> Zhi Zhang,<sup>2</sup> Yingchao Du,<sup>2</sup> Wenhui Huang,<sup>2</sup> and Chuanxiang Tang<sup>2</sup>

<sup>1</sup>Key Laboratory of Beam Technology of Ministry of Education,  
School of Physics and Astronomy, Beijing Normal University, Beijing 100875, China  
<sup>2</sup>Key Laboratory of Particle and Radiation Imaging of Ministry of Education,  
Department of Engineering Physics, Tsinghua University, Beijing 100084, China

Gamma-ray spectral computed tomography (CT) plays a crucial role in the discrimination of heavy metal materials, as it provides detailed information on atomic composition, including electron density  $\rho_e$  and effective atomic number  $Z_{\text{eff}}$ . However, the reconstruction accuracy of  $\rho_e$  and  $Z_{\text{eff}}$  in conventional gamma-ray dual-energy CT is constrained by the use of bremsstrahlung spectra and the omission of the photoelectric effect term in the decomposition of the linear attenuation coefficient. To improve the reconstruction accuracy of  $\rho_e$  and  $Z_{\text{eff}}$ , a triple-energy CT method based on an inverse Compton scattering (ICS) gamma-ray source was proposed in this paper, and its validity was demonstrated via Monte Carlo simulations. By utilizing the quasi-monochromatic and continuously energy-tunable gamma-rays generated by an ICS light source, the contributions of the photoelectric effect, Compton scattering, and pair production to the linear attenuation coefficient of an imaging material can all be accurately accounted for, which enables the decomposition of the linear attenuation coefficient of an unknown material using three basis materials. Compared to gamma-ray dual-energy CT, the gamma-ray triple-energy CT developed in this study significantly enhances the reconstruction accuracy of  $\rho_e$  and  $Z_{\text{eff}}$ . A phantom study revealed that the gamma-ray triple-energy CT enables the retrieval of  $\rho_e$  and  $Z_{\text{eff}}$  with reconstruction accuracies exceeding 1% and 3.5%, respectively.

Keywords: Gamma-ray spectral computed tomography, Electron density, Effective atomic number, Inverse Compton scattering light source, Monte Carlo simulation

## I. INTRODUCTION

Owing to its strong penetration capability, gamma-rays with photon energies above 100 keV play a crucial role in medical, industrial, and security imaging applications. Gamma-rays are typically generated through two primary methods: the decay of radioactive isotopes (e.g.,  $^{60}\text{Co}$ ,  $^{137}\text{Cs}$ ,  $^{99\text{m}}\text{Tc}$ ,  $^{131}\text{I}$ ,  $^{18}\text{F}$ , etc.) and the bremsstrahlung radiation produced by high-energy electrons. The former method can generate a monochromatic gamma-ray spectrum, but the spatial distribution of the gamma-rays is isotropic. As a result, it is primarily utilized as an emission source in nuclear medicine imaging, including single photon emission computed tomography (SPECT) [1, 2] and positron emission tomography (PET) [3–5]. The latter method generates gamma-rays with a specific directionality, making it widely applicable in conventional transmission imaging. However, the gamma-ray spectrum produced by this approach is highly broad, with photon energies spanning from zero up to the maximum energy of the incident electrons. When using the broad bremsstrahlung spectrum for imaging, different materials can exhibit identical attenuation characteristics [6, 7], making them indistinguishable. Since the gamma-ray attenuation of a material is energy-dependent, spectral radiography holds significant potential for enhancing material discrimination capabilities. As a result, dual-energy radiography has been widely adopted in

practical applications. The primary limitation of dual-energy radiography is its difficulty in distinguishing between materials when they are stacked together. Although methods such as the virtual peeling technique [8] and dynamic material discrimination algorithm [9] have been developed to address material overlap issues, their performance is significantly compromised by nonuniform or coarse-textured backgrounds.

To completely resolve the material overlap problem, computed tomography (CT) technique must be adopted, as it can generate cross-sectional attenuation images of an object by capturing radiographs from multiple angles around the object. When dual-energy CT is employed, the atomic composition information of an imaging object—including electron density  $\rho_e$  and effective atomic number  $Z_{\text{eff}}$ —can be obtained in addition to the linear attenuation coefficient, significantly enhancing the capability for material discrimination. Furthermore, the information on  $\rho_e$  and  $Z_{\text{eff}}$  can also enhance the accuracy of dose calculation [10–12] and range estimation [13–17] in proton and heavy-ion therapy. In dual-energy CT, the two energy spectra can be generated either at the source level (e.g., via dual-source configurations [18, 19] or fast kVp/MVp switching [20–22]) or at the detector level (e.g., employing a sandwich detector design [23, 24]). In each scenario, the energy spectra are inherently broad. The application of such broad spectra leads to beam hardening artifacts in CT reconstruction [22, 25], which severely impacts the quantitative analysis of the results. Additionally, a conventional bremsstrahlung-based gamma-ray source can produce at most two energy spectra. As a result, the contribution of the photoelectric effect to the linear attenuation coefficient of an imaging material is often neglected in gamma-ray dual-energy CT [22, 26], resulting in substantial errors, particu-

\* Supported by the National Natural Science Foundation of China (Grant Nos. 12375157, 12027902, and 11905011).

† [chizj18@bnu.edu.cn](mailto:chizj18@bnu.edu.cn)

larly for high-Z materials. For instance, the photoelectric effect contributes more than 20% to the total attenuation of lead (Pb) at a gamma-ray energy of 1 MeV, as shown in Fig. 1. Although photon-counting detectors enable multi-energy CT in the low-energy range (10–100 keV) [28–30], this technique is difficult to extend to the high-energy region (100 keV to several MeV). Consequently, gamma-ray multi-energy CT has not been achieved.

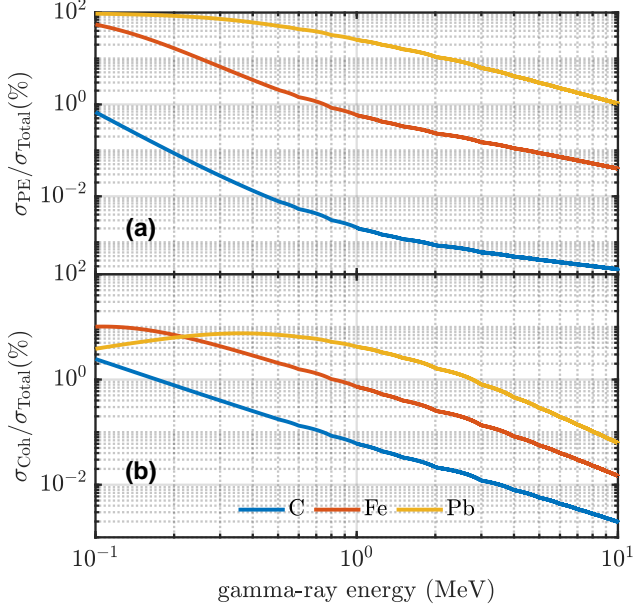


Fig. 1. Contributions of the photoelectric effect (a) and coherent scattering (b) to the linear attenuation coefficient for various materials. The interaction cross sections  $\sigma_{PE}$ ,  $\sigma_{Coh}$ , and  $\sigma_{Total}$  represent the contributions from the photoelectric effect, coherent scattering, and the total attenuation, respectively. For high-Z materials, the coherent scattering cross section is significantly smaller than that of the photoelectric effect, making its contribution to the total attenuation negligible. However, the photoelectric effect's contribution cannot be ignored, even in the MeV energy range, as its omission would introduce significant errors in the decomposition of the linear attenuation coefficient. Data were obtained using the XOP software [31].

As an alternative, an inverse Compton scattering (ICS) light source, based on the collision between a relativistic electron beam and a laser, can generate quasi-monochromatic and continuously energy-tunable gamma-rays with high brightness [32–35], which makes it an ideal light source for gamma-ray spectral CT imaging. The gamma-rays generated by an ICS light source can span an energy range from tens of keV to several MeV, fulfilling the requirements for biomedical imaging and material nondestructive testing. In the X-ray energy region (below 100 keV), the ICS light source has proven to be a vital tool for spectral imaging, such as K-edge subtraction (KES) [36–38] and dual-energy CT [39]. However, in the gamma-ray energy region (100 keV to several MeV), spectral imaging based on an ICS light source remains largely unexplored.

In this paper, we propose a gamma-ray spectral CT method based on an ICS light source. By employing triple-energy CT

scanning instead of the conventional dual-energy approach, the electron density  $\rho_e$  and effective atomic number  $Z_{eff}$  of an imaging object can be reconstructed with significantly higher accuracy. The feasibility and validity of this gamma-ray spectral CT method were demonstrated through Monte Carlo simulations.

## II. METHODS

### A. Physical model of gamma-ray triple-energy CT

Gamma-ray attenuation in an imaging material is governed by four interaction mechanisms: Rayleigh (coherent) scattering, the photoelectric effect, Compton (incoherent) scattering, and pair production. However, the contribution of coherent scattering is typically negligible compared to the other mechanisms, as illustrated in Fig. 1. Therefore, in practical applications, only the latter three effects—the photoelectric effect, Compton scattering, and pair production—are usually considered. The interaction cross sections of the photoelectric effect, Compton (incoherent) scattering, and pair production are all energy-dependent. For the photoelectric effect, the energy-dependence  $f_{PE}(E)$  is empirically approximated as  $1/E^\kappa$  in the absence of electron-shell discontinuities, with the constant  $\kappa$  typically set to  $\sim 3$  or lower as the gamma-ray energy increases [40]. For Compton scattering, the energy-dependence  $f_{CS}(E)$ , assuming unbound electrons at rest, is described by the well-known Klein-Nishina formula, neglecting the incoherent scattering function and Doppler broadening. For pair production, the energy-dependence  $f_{PP}(E)$  is highly complex and is often simplified using a crude model (e.g.,  $\propto E$  [22]). The energy-dependencies  $f_{PE}(E)$ ,  $f_{CS}(E)$ , and  $f_{PP}(E)$  can serve as basis functions for the energy-dependent decomposition of the linear attenuation coefficient  $\mu(E)$  of an imaging object, expressed as:

$$\mu(E) = a_{PE}f_{PE}(E) + a_{CS}f_{CS}(E) + a_{PP}f_{PP}(E), \quad (1)$$

where the decomposition coefficients  $a_{PE}$ ,  $a_{CS}$ , and  $a_{PP}$  are directly related to the material properties,

$$a_{PE} = K_1 Z^n \rho \frac{Z}{A}, \quad (2a)$$

$$a_{CS} = K_2 \rho \frac{Z}{A}, \quad (2b)$$

$$a_{PP} = K_3 Z \rho \frac{Z}{A}, \quad (2c)$$

where  $\rho$ ,  $Z$ , and  $A$  represent the mass density, atomic number, and atomic weight, respectively,  $K_1$ ,  $K_2$ , and  $K_3$  are constants typically determined through calibration using materials of interest with known properties in practical applications, and  $n$  is approximately 3 for high-Z materials and 3.8 for low-Z materials [40].

To determine the three decomposition coefficients  $a_{PE}$ ,  $a_{CS}$ , and  $a_{PP}$ , CT scans at three photon energies are required. However, conventional dual-energy CT can provide at most two energy spectra. In practice, only two of these coefficients are calculated by neglecting either pair production in the keV energy region or the photoelectric effect in the MeV energy region. In the keV energy region, pair production cannot occur because the photon energy is below the threshold of 1.022 MeV, making its omission **straightforward**. However, in the MeV energy region, the neglecting of the photoelectric effect introduces significant errors, particularly for high-Z materials, as demonstrated in Fig. 1. Therefore, triple-energy CT is essential for the accurate reconstruction of these decomposition coefficients.

Alternatively, the energy-dependent linear attenuation coefficient  $\mu(E)$  of an imaging object can be decomposed using three basis materials (BM1, BM2, and BM3) instead of the aforementioned basis functions, as follows:

$$\mu(E) = c_1\mu_{BM,1}(E) + c_2\mu_{BM,2}(E) + c_3\mu_{BM,3}(E), \quad (3)$$

where  $\mu_{BM,i}(E)$  ( $i = 1, 2$ , or  $3$ ) represents the linear attenuation coefficient of the  $i$ th basis material, whose values are known at different gamma-ray energies, and  $c_i$  ( $i = 1, 2$ , or  $3$ ) denotes the decomposition coefficient, which is related to the decomposition coefficients  $a_{PE,i}$ ,  $a_{CS,i}$ , and  $a_{PP,i}$  ( $i = 1, 2$ , or  $3$ ) of the  $i$ th material as follows:

$$c_1 = \frac{1}{|\mathbb{A}|} \begin{vmatrix} a_{PE} & a_{PE,2} & a_{PE,3} \\ a_{CS} & a_{CS,2} & a_{CS,3} \\ a_{PP} & a_{PP,2} & a_{PP,3} \end{vmatrix}, \quad (4a)$$

$$c_2 = \frac{1}{|\mathbb{A}|} \begin{vmatrix} a_{PE,1} & a_{PE} & a_{PE,3} \\ a_{CS,1} & a_{CS} & a_{CS,3} \\ a_{PP,1} & a_{PP} & a_{PP,3} \end{vmatrix}, \quad (4b)$$

$$c_3 = \frac{1}{|\mathbb{A}|} \begin{vmatrix} a_{PE,1} & a_{PE,2} & a_{PE} \\ a_{CS,1} & a_{CS,2} & a_{CS} \\ a_{PP,1} & a_{PP,2} & a_{PP} \end{vmatrix}, \quad (4c)$$

with the coefficient matrix

$$\mathbb{A} = \begin{bmatrix} a_{PE,1} & a_{PE,2} & a_{PE,3} \\ a_{CS,1} & a_{CS,2} & a_{CS,3} \\ a_{PP,1} & a_{PP,2} & a_{PP,3} \end{bmatrix}. \quad (5)$$

This three-basis-material decomposition of  $\mu(E)$  generalizes the two-basis-material approach employed in conventional dual-energy CT [26], which is limited to calculating two decomposition coefficients using two energy spectra.

When three gamma-ray spectra are utilized for the CT scan, projections of the linear attenuation coefficient at high, middle, and low gamma-ray energies can be obtained,

$$P_H = -\ln \int_{\text{SpecH}} S(E) \exp \left[ -\int_s \mu(\vec{r}, E) ds \right] dE, \quad (6a)$$

$$P_M = -\ln \int_{\text{SpecM}} S(E) \exp \left[ -\int_s \mu(\vec{r}, E) ds \right] dE, \quad (6b)$$

$$P_L = -\ln \int_{\text{SpecL}} S(E) \exp \left[ -\int_s \mu(\vec{r}, E) ds \right] dE, \quad (6c)$$

where  $P_H$ ,  $P_M$  and  $P_L$  represent the measured projections at high-energy (SpecH), middle-energy (SpecM) and low-energy (SpecL) spectra, respectively,  $\vec{r}$  is an arbitrary position vector in Euclidean space, and  $S(E)$  denotes the intensity-normalized energy spectrum, satisfying  $\int_{\text{SpecH}} S(E) dE = \int_{\text{SpecM}} S(E) dE = \int_{\text{SpecL}} S(E) dE = 1$ . **For an ICS light source, the energy distribution is angular-dependent [27, 45]. To reduce the energy spectrum to its intrinsic form, a large source-to-sample distance—typically on the order of several tens of meters—must be employed.** The intrinsic energy spectrum, which depends solely on the electron and laser beam parameters rather than the collecting angle, can be approximated by a Gaussian distribution, with a typically narrow bandwidth (e.g., an rms value of a few percent). When an ICS light source is utilized for triple-energy CT, the normalized energy spectrum  $S(E)$  in Eq. (6), compared to the energy dependence of  $\mu(E)$  in the gamma-ray energy region, can be approximated as a Dirac function  $\delta(E)$ . Thus, Eq. (6) can be simplified as follows:

$$P_H = \int_s \mu(\vec{r}, E_H) ds, \quad (7a)$$

$$P_M = \int_s \mu(\vec{r}, E_M) ds, \quad (7b)$$

$$P_L = \int_s \mu(\vec{r}, E_L) ds, \quad (7c)$$

where  $E_H$ ,  $E_M$ , and  $E_L$  represent the peak energies of the high-, middle-, and low-energy spectra, respectively. Using Eq. (7), the linear attenuation coefficients  $\mu(E_H)$ ,  $\mu(E_M)$ , and  $\mu(E_L)$  of the imaging object can be reconstructed. The reconstruction method employed in this study is the Algebraic Reconstruction Technique with Total Variation (ART-TV) iterative algorithm. Thus, the decomposition coefficients  $c_1$ ,  $c_2$ , and  $c_3$  can be determined by solving the following linear equation system:

$$\mathbb{M} \begin{bmatrix} c_1 \\ c_2 \\ c_3 \end{bmatrix} = \begin{bmatrix} \mu(E_H) \\ \mu(E_M) \\ \mu(E_L) \end{bmatrix}, \quad (8)$$

with the coefficient matrix

$$\mathbb{M} = \begin{bmatrix} \mu_{BM,1}(E_H) & \mu_{BM,2}(E_H) & \mu_{BM,3}(E_H) \\ \mu_{BM,1}(E_M) & \mu_{BM,2}(E_M) & \mu_{BM,3}(E_M) \\ \mu_{BM,1}(E_L) & \mu_{BM,2}(E_L) & \mu_{BM,3}(E_L) \end{bmatrix}. \quad (9)$$

This method for determining  $c_i$  ( $i = 1, 2$ , and  $3$ ) is known as the post-processing method. Additionally, these decomposition coefficients can be calculated in another way. By substituting Eq. (3) into Eq. (7), a different linear equation system

can be established,

$$\mathbb{M} \begin{bmatrix} C_1 \\ C_2 \\ C_3 \end{bmatrix} = \begin{bmatrix} P_H \\ P_M \\ P_L \end{bmatrix}, \quad (10)$$

with

$$C_1 = \int_s c_1(\vec{r}) ds, \quad (11a)$$

$$C_2 = \int_s c_2(\vec{r}) ds, \quad (11b)$$

$$C_3 = \int_s c_3(\vec{r}) ds, \quad (11c)$$

denoting the projections of  $c_1$ ,  $c_2$ , and  $c_3$ , respectively. By solving Eq. (10), the projections  $C_1$ ,  $C_2$ , and  $C_3$  can be obtained. Using these projections, the decomposition coefficients  $c_1$ ,  $c_2$ , and  $c_3$  can also be reconstructed through the ART-TV iterative algorithm. This method for determining  $c_i$  ( $i = 1, 2$ , and  $3$ ) is known as the pre-processing method.

## B. Electron density and effective atomic number retrieval

Combining Eqs. (1) and (2), the linear attenuation coefficient of an imaging object can be written in the following form:

$$\mu(E) = K_1 Z_{\text{eff}}^n \rho_e f_{\text{PE}}(E) + K_2 \rho_e f_{\text{CS}}(E) + K_3 Z_{\text{eff}} \rho_e f_{\text{PP}}(E), \quad (12)$$

where the effective atomic number  $Z_{\text{eff}}$ , rather than the atomic number  $Z$ , is used to account for any material, particularly composite materials, and  $\rho_e$  represents the electron density, defined as

$$\rho_e = \rho \frac{Z}{A} N_A, \quad (13)$$

with  $N_A$  denoting the Avogadro's constant. Through the simultaneous solution of Eqs. (12) and (3), along with expressing the linear attenuation coefficients of the three basis materials in terms of Eq. (12), the electron density  $\rho_e$  and effective atomic number  $Z_{\text{eff}}$  of an imaging object can be easily determined,

$$\rho_e = c_1 \rho_{e,1} + c_2 \rho_{e,2} + c_3 \rho_{e,3}, \quad (14a)$$

$$Z_{\text{eff}} = \frac{c_1 Z_1 \rho_{e,1} + c_2 Z_2 \rho_{e,2} + c_3 Z_3 \rho_{e,3}}{\rho_e}, \quad (14b)$$

where  $\rho_{e,i}$  and  $Z_i$  ( $i = 1, 2$ , or  $3$ ) represent the electron density and atomic number of the  $i$ th basis material, respectively. For more accurate calculations of  $\rho_e$  and  $Z_{\text{eff}}$ , our previous studies demonstrated that the post-processing method

offers a clear advantage for  $\rho_e$  reconstruction, while the pre-processing method is preferred for  $Z_{\text{eff}}$  reconstruction [41]. This conclusion is applied in the subsequent retrieval of  $\rho_e$  and  $Z_{\text{eff}}$ .

If dual-energy spectra with gamma-ray peak energies of  $E_H$  and  $E_L$ , instead of triple-energy spectra, generated by an ICS light source are used for the CT scan, the electron density  $\rho_e$  and effective atomic number  $Z_{\text{eff}}$  of an imaging object can still be retrieved by neglecting the photoelectric term in Eq. (1) and utilizing only two basis materials (e.g., BM1 and BM2) in Eq. (3),

$$\rho_e = c'_1 \rho_{e,1} + c'_2 \rho_{e,2}, \quad (15a)$$

$$Z_{\text{eff}} = \frac{c'_1 Z_1 \rho_{e,1} + c'_2 Z_2 \rho_{e,2}}{\rho_e}, \quad (15b)$$

where the coefficients  $c'_1$  and  $c'_2$  can be determined either by solving the linear equation system

$$\mathbb{B}' \begin{bmatrix} c'_1 \\ c'_2 \end{bmatrix} = \begin{bmatrix} \mu(E_H) \\ \mu(E_L) \end{bmatrix} \quad (16)$$

(post-processing method) or through CT reconstruction using the projections  $C'_1$  and  $C'_2$ , which are obtained by solving the linear equation system

$$\mathbb{B}' \begin{bmatrix} C'_1 \\ C'_2 \end{bmatrix} = \begin{bmatrix} P_H \\ P_L \end{bmatrix} \quad (17)$$

(pre-processing method), with

$$\mathbb{B}' = \begin{bmatrix} \mu_{\text{BM},1}(E_H) & \mu_{\text{BM},2}(E_H) \\ \mu_{\text{BM},1}(E_L) & \mu_{\text{BM},2}(E_L) \end{bmatrix}. \quad (18)$$

## C. Monte Carlo simulation

To demonstrate the feasibility of high-accuracy  $\rho_e$  and  $Z_{\text{eff}}$  retrieval using gamma-ray triple-energy CT, Monte Carlo (MC) simulations were conducted using the Geant4 toolkit [42]. The imaging layout is illustrated in Fig. 2. A fan-beam geometry and a linear detector were employed in the simulation. The gamma-ray source was modeled based on the very compact ICS gamma-ray source (VIGAS) [43, 44] currently under construction at Tsinghua university. The three gamma-ray spectra were modeled as Gaussian distributions with peak energies of  $E_H = 4$  MeV,  $E_M = 2$  MeV, and  $E_L = 1$  MeV, each with an rms bandwidth of 1.5%. To satisfy the field-of-view (FOV) requirement of the imaging object ( $\sim 3$  cm) while maintaining the quasi-monochromaticity of the incident gamma-rays (1.5% rms bandwidth), a large source-to-sample distance—typically tens of meters for MeV gamma-rays—is necessary for an ICS light source, as the gamma-ray peak energy is angular-dependent [45]. To avoid unnecessary gamma-ray transport before reaching the phantom, a two-dimensional (2D) quasi-parallel gamma-ray beam was used in the MC simulation. The incident gamma-rays were detected



by an ideal transmission detector (100% detection efficiency and free of electronic noise) positioned 0.5 m downstream of the phantom. The spatial resolution of the transmission detector was modeled based on the imaging detector under development at the VIGAS, with a pixel size of 0.2 mm.

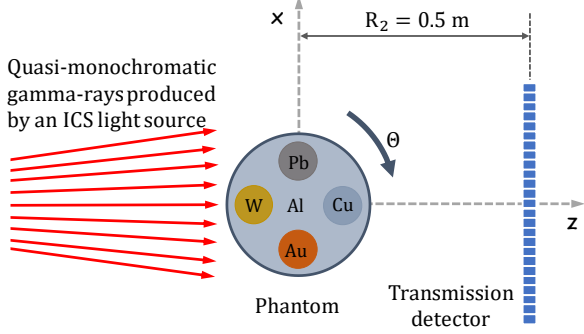


Fig. 2. Imaging layout for gamma-ray triple-energy CT using an ICS light source (not to scale).

The phantom was designed as an aluminum (Al) cylinder with a diameter of 3.0 cm, containing four inner cylindrical columns, each with a diameter of 0.8 cm. The materials of the inner columns were lead (Pb), tungsten (W), gold (Au), and copper (Cu), respectively. The phantom was centered within the 2D quasi-parallel gamma-ray beam and rotated around the central axis of the Al cylinder during the spectral CT scan.

In the MC simulation, the Geant4 physics list was configured as follows: for gamma photons, all relevant interaction processes—including Rayleigh scattering, the photoelectric effect, Compton scattering, and pair production—were fully incorporated using the Livermore model; for both electrons and positrons, interaction processes including multiple scattering, ionization, and bremsstrahlung were comprehensively modeled, with the annihilation process explicitly included for positrons; furthermore, a range cutoff value of 1  $\mu\text{m}$  was applied to gamma photons, electrons, and positrons. For each gamma-ray spectrum CT scan, 180 projections were collected at 1° angular intervals. To achieve a balance between computational time and statistical accuracy, the number of incident gamma-ray photons was set to  $2 \times 10^8$  for each projection.

### III. RESULTS AND DISCUSSIONS

The monochromatic CT reconstruction results of the phantom are displayed in Fig. 3. In the MeV energy range, the linear attenuation coefficients of W and Au are very similar, rendering the two columns almost indistinguishable in the attenuation CT images. For quantitative analysis, five regions-of-interest (ROIs), indicated by white dotted squares in Fig. 3(c), were selected. The reconstructed linear attenuation coefficients for the five materials in the phantom, including their mean values and corresponding standard errors, are summarized in Table 1. Also given in Table 1 are the theoretical

values of the linear attenuation coefficients and the relative error (RE) values. Given the quasi-monochromatic nature of the gamma-ray spectra from the VIGAS used in the MC simulation (1.5% rms bandwidth, Gaussian distribution), the reconstruction results show excellent agreement with the theoretical values for all materials except Al, with relative errors below 1% for the three gamma-ray spectra. The larger relative errors observed for Al at the three gamma-ray spectra are primarily attributed to horizontal streaks around the top and bottom regions of the circular inserts in the reconstructed CT images. These streaks are metal artifacts caused by the low spatial resolution of the transmission detector, particularly pronounced for high-Z materials.

The three basis materials used for decomposing the linear attenuation coefficient are aluminum (Al), iron (Fe), and lead (Pb). The linear attenuation coefficients, electron densities, and atomic numbers of these basis materials are available from the National Institute of Standards and Technology (NIST) [46]. Using the three monochromatic CT images of the phantom, the decomposition coefficients in Eq. (3) were calculated via the post-processing method. Subsequently, the electron density  $\rho_e$  image of the phantom was reconstructed using Eq. (14a), as shown in Fig. 4(a). Additionally, the decomposition coefficients in Eq. (3) were also computed using the pre-processing method described in Section II A. Based on these coefficients, the effective atomic number  $Z_{\text{eff}}$  image of the phantom was retrieved using Eq. (14b), with the result shown in Fig. 4(b). Compared to the attenuation  $\mu$  images, the  $\rho_e$  and  $Z_{\text{eff}}$  images of the phantom exhibit significantly different contrast. In the  $\rho_e$  image, Cu and Pb are nearly indistinguishable, whereas they are clearly differentiated in the  $\mu$  and  $Z_{\text{eff}}$  images. Furthermore, W and Au show similar contrast in the  $\mu$  and  $\rho_e$  images but become distinguishable in the  $Z_{\text{eff}}$  image.

To quantitatively analyze the reconstruction results of  $\rho_e$  and  $Z_{\text{eff}}$ , the ROIs selected in Fig. 3(c) were also used. The reconstructed  $\rho_e$  and  $Z_{\text{eff}}$  values of the phantom, along with their theoretical values, are provided in Tables 2 and 3, respectively. Both  $\rho_e$  and  $Z_{\text{eff}}$  for the five materials in the phantom were accurately retrieved. For all five materials, the relative errors of  $\rho_e$  were all less than 1%, and the maximum relative error of  $Z_{\text{eff}}$  was below 3.5%. Compared to  $\rho_e$ , the reconstruction accuracy of  $Z_{\text{eff}}$  was slightly lower. This can be attributed to the division operation in Eq. (14b), which amplifies errors in the  $\rho_e$  image and results in a noisier  $Z_{\text{eff}}$  image, as shown in Fig. 4(b).

For comparison, the  $\rho_e$  and  $Z_{\text{eff}}$  images of the phantom were also reconstructed using dual-energy CT with gamma-ray peak energies of  $E_H = 4$  MeV and  $E_L = 1$  MeV, as shown in Fig. 5. Although the  $\rho_e$  and  $Z_{\text{eff}}$  images of the phantom exhibit accurate spatial identification, the quantitative results are less reliable, particularly for  $Z_{\text{eff}}$ . For instance, the  $Z_{\text{eff}}$  values of Pb, W, and Au in Fig. 5(d) are negative, which is physically unrealistic. For quantitative comparison, the ROIs selected in Fig. 3(c) were also used. The  $\rho_e$  and  $Z_{\text{eff}}$  retrieval results from gamma-ray dual-energy CT are given in Tables 2 and 3, respectively. In gamma-ray dual-energy CT, the retrieval accuracy of  $\rho_e$  and  $Z_{\text{eff}}$  is heavily influenced by

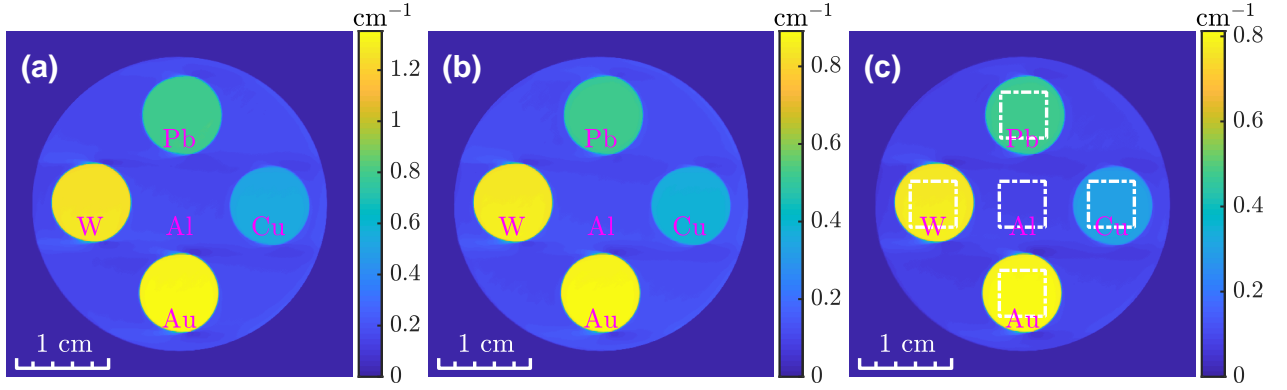


Fig. 3. CT reconstruction results of the phantom at gamma-ray peak energies of (a) 4 MeV, (b) 2 MeV, and (c) 1 MeV. The white dotted squares in (c) indicate the ROIs selected for quantitative analysis of the reconstruction results.

TABLE 1. Reconstructed linear attenuation coefficients of the five materials in the phantom.

Material	1 MeV			2 MeV			4 MeV		
	Recon. value (cm <sup>-1</sup> )	Ref. value (cm <sup>-1</sup> )	RE (%)	Recon. value (cm <sup>-1</sup> )	Ref. value (cm <sup>-1</sup> )	RE (%)	Recon. value (cm <sup>-1</sup> )	Ref. value (cm <sup>-1</sup> )	RE (%)
Al	0.171±0.010	0.165	3.17	0.119±0.007	0.116	2.33	0.086±0.007	0.084	2.88
Cu	0.528±0.013	0.527	0.18	0.376±0.008	0.375	0.04	0.296±0.007	0.296	0.25
Pb	0.797±0.004	0.800	0.40	0.517±0.003	0.520	0.57	0.472±0.002	0.475	0.72
W	1.264±0.008	1.268	0.35	0.848±0.006	0.852	0.51	0.773±0.005	0.777	0.61
Au	1.333±0.010	1.334	0.04	0.878±0.005	0.879	0.05	0.801±0.006	0.803	0.26

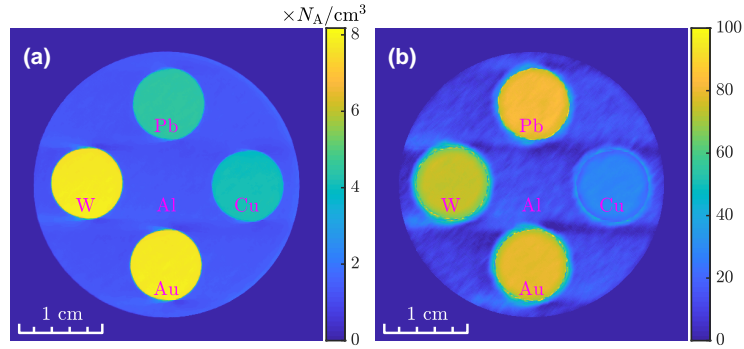


Fig. 4. Electron density  $\rho_e$  (a) and effective atomic number  $Z_{\text{eff}}$  (b) images of the phantom reconstructed using gamma-ray triple-energy CT.

TABLE 2. Retrieved electron density  $\rho_e$  of the phantom using gamma-ray triple-energy and dual-energy CT.

Material	Ref. value ( $\times N_A \text{ cm}^{-3}$ )	Three-energy CT		Dual-energy CT with different basis-material choices					
		Recon. value ( $\times N_A \text{ cm}^{-3}$ )	RE (%)	Al and Fe		Al and Pb		Fe and Pb	
				Recon. value ( $\times N_A \text{ cm}^{-3}$ )	RE (%)	Recon. value ( $\times N_A \text{ cm}^{-3}$ )	RE (%)	Recon. value ( $\times N_A \text{ cm}^{-3}$ )	RE (%)
Al	1.300	1.313±0.069	0.98	1.342±0.079	3.20	1.348±0.049	3.64	1.766±0.042	35.82
Cu	4.089	4.087±0.075	0.05	4.107±0.097	0.44	3.418±0.085	16.41	3.906±0.110	4.48
Pb	4.492	4.456±0.036	0.80	6.161±0.033	37.17	4.513±0.030	0.47	4.555±0.041	1.40
W	7.768	7.738±0.061	0.39	9.740±0.064	25.38	6.540±0.073	15.81	5.940±0.123	23.53
Au	7.749	7.775±0.026	0.33	10.293±0.075	32.83	7.261±0.060	6.30	7.018±0.071	9.43

the choice of basis materials. When Al and Fe are selected over, the  $Z_{\text{eff}}$  retrieval results for these non-basis materials are as basis materials, the relative error of  $\rho_e$  exceeds 20% for even worse, with relative errors exceeding 140%. However, high-Z non-basis materials, including Pb, W, and Au. More- when Al and Pb are chosen as basis materials, the  $\rho_e$  retrieval

TABLE 3. Retrieved effective atomic number  $Z_{\text{eff}}$  of the phantom using gamma-ray triple-energy and dual-energy CT.

Material	Ref. value	Three-energy CT		Dual-energy CT with different basis-material choices					
		Recon. value	RE (%)	Al and Fe		Al and Pb		Fe and Pb	
				Recon. value	RE (%)	Recon. value	RE (%)	Recon. value	RE (%)
Al	13	$12.86 \pm 2.08$	1.05	$14.07 \pm 5.00$	8.25	$17.22 \pm 2.15$	32.45	$28.65 \pm 0.33$	120.41
Cu	29	$28.02 \pm 1.04$	3.39	$26.81 \pm 3.21$	7.56	$7.60 \pm 0.97$	73.78	$30.18 \pm 0.33$	4.08
Pb	82	$80.26 \pm 1.41$	2.12	$-67.19 \pm 2.94$	181.94	$80.71 \pm 0.92$	1.58	$82.41 \pm 0.96$	0.50
W	74	$73.22 \pm 1.37$	1.06	$-36.33 \pm 1.11$	149.10	$59.96 \pm 1.93$	18.97	$78.93 \pm 2.34$	6.66
Au	79	$77.39 \pm 1.16$	2.03	$-56.79 \pm 2.24$	171.89	$73.55 \pm 1.22$	6.90	$81.03 \pm 1.12$	2.57

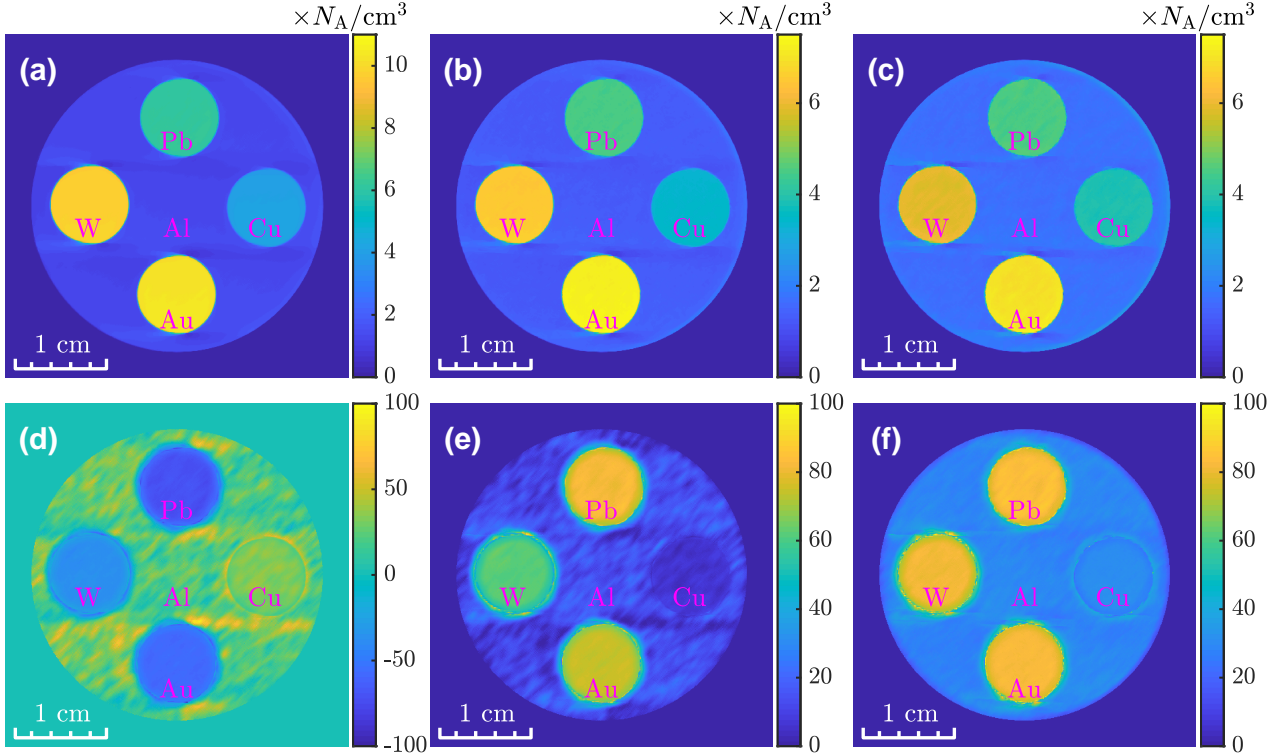


Fig. 5. Electron density  $\rho_e$  (a, b, c) and effective atomic number  $Z_{\text{eff}}$  (d, e, f) images of the phantom reconstructed using gamma-ray dual-energy CT with different basis-material combinations: (a, d) Al and Fe, (b, e) Al and Pb, and (c, f) Fe and Pb.

accuracy for non-basis materials can be reduced to less than 20%. Similarly, when Fe and Pb are selected as basis materials, the  $Z_{\text{eff}}$  retrieval accuracy for non-basis materials (except Al) can be improved to less than 10%. As expected, the  $\rho_e$  and  $Z_{\text{eff}}$  of basis materials are consistently retrieved with higher accuracy compared to non-basis materials. Notably, the  $\rho_e$  and  $Z_{\text{eff}}$  of Cu can be accurately retrieved when Fe is included as one of the basis materials, owing to the similar attenuation characteristics of Cu and Fe in this energy range [ $\mu_{\text{Cu}}(E) \simeq Z_{\text{Cu}}/Z_{\text{Fe}}\mu_{\text{Fe}}(E)$ ]. Compared to gamma-ray dual-energy CT, the retrieval accuracy of  $\rho_e$  and  $Z_{\text{eff}}$  is significantly improved using gamma-ray triple-energy CT, as demonstrated in Tables 2 and 3. By including low-Z (Al), moderate-Z (Fe), and high-Z (Pb) materials as basis materials, an arbitrary material in the phantom can be more accurately approximated by a combination of these three basis materials,

rather than just two, resulting in higher precision.

Due to the division operation involved in  $Z_{\text{eff}}$  retrieval in Eqs. (14b) and (15b), the  $Z_{\text{eff}}$  retrieval results for the phantom are less accurate than those of  $\rho_e$  for both dual-energy and triple-energy CT. Additionally, influenced by metal artifacts in the attenuation CT images, the  $Z_{\text{eff}}$  retrieval precision (standard error) for Al is worse compared to the other four materials in the phantom. For high-quality  $Z_{\text{eff}}$  image retrieval, deep learning techniques have been proven to be an effective approach [47]. By leveraging deep learning, gamma-ray triple-energy CT has the potential to achieve even higher accuracy in  $Z_{\text{eff}}$  retrieval. The retrieval of  $Z_{\text{eff}}$  can also be achieved through various methods, such as the theoretical calculation [48, 49], the Compton backscattering method [50], and the estimation of mass collision stopping power based on charged particles [51]. Although these meth-

ods are straightforward to implement, they are either limited to materials with known compositions [48, 49] or unable to resolve the retrieval of  $Z_{\text{eff}}$  for each material in cases where different materials overlap [50, 51]. The gamma-ray triple-energy CT method proposed in this work effectively addresses the aforementioned limitations and achieves accurate retrieval of  $Z_{\text{eff}}$  for imaging materials. This advancement will significantly improve the accuracy of material identification, radiation shielding design, and radiation dose calculation.

#### IV. CONCLUSION

An inverse Compton scattering (ICS) light source serves as an exceptional tool for gamma-ray spectral computed tomography (CT), as it is capable of producing quasi-

monochromatic, continuously energy-tunable, and high-brightness gamma-rays. With an ICS light source, gamma-ray triple-energy CT can be easily achieved. By exploiting triple-energy CT, the linear attenuation coefficient of an imaging object can be decomposed into three components, either through three basis functions derived from photoelectric, Compton scattering, and pair production effects or via three basis materials, thereby extending the capabilities of conventional dual-energy CT. By selecting low-, moderate-, and high-Z materials as basis materials, the electron density  $\rho_e$  and effective atomic number  $Z_{\text{eff}}$  of an imaging object can be accurately retrieved. The efficacy of gamma-ray triple-energy CT based on an ICS light source has been validated through Monte Carlo (MC) simulations. The simulation results demonstrate that  $\rho_e$  and  $Z_{\text{eff}}$  can be retrieved with accuracies better than 1% and 3.5%, respectively.

- [1] M.T. Madsen, Recent advances in SPECT imaging. *J. Nucl. Med.* **48**, 661-673 (2007). doi: [10.2967/jnumed.106.032680](https://doi.org/10.2967/jnumed.106.032680)
- [2] M.M. Khalil, J.L. Tremoleda, T.B. Bayomy et al, Molecular SPECT imaging: an overview. *Int. J. Mol. Imaging* **2011**, 796025 (2011). doi: [10.1155/2011/796025](https://doi.org/10.1155/2011/796025)
- [3] S.M. Ametamey, M. Honer, P.A. Schubiger, Molecular imaging with PET. *Chem. Rev.* **108**, 1501-1516 (2008). doi: [10.1021/cr0782426](https://doi.org/10.1021/cr0782426)
- [4] V. Pichler, N. Berroterán-Infante, C Philippe et al, An overview of PET radiochemistry, part 1: the covalent labels  $^{18}\text{F}$ ,  $^{11}\text{C}$ , and  $^{13}\text{N}$ . *J. Nucl. Med.* **59**, 1350-1354 (2018). doi: [10.2967/jnumed.117.190793](https://doi.org/10.2967/jnumed.117.190793)
- [5] M. Brandt, J. Cardinale, M.L. Aulsebrook et al, An overview of PET radiochemistry, part 2: Radiometals. *J. Nucl. Med.* **59**, 1500-1506 (2018). doi: [10.2967/jnumed.117.190801](https://doi.org/10.2967/jnumed.117.190801)
- [6] K. Taguchi, J.S. Iwanczyk, Vision 20/20: single photon counting x-ray detectors in medical imaging. *Med. Phys.* **40**, 100901 (2013). doi: [10.1118/1.4820371](https://doi.org/10.1118/1.4820371)
- [7] C.H. McCollough, S. Leng, L.F. Yu et al, Dual-and multi-energy CT: principles, technical approaches, and clinical applications. *Radiology* **276**, 637-653 (2015). doi: [10.1148/radiol.2015142631](https://doi.org/10.1148/radiol.2015142631)
- [8] G.Y. Chen, J. Turnera, D. Nisius et al, Linatron mi6, the x-ray source for cargo inspection. *Phys. Procedia* **66**, 68-74 (2015). doi: [10.1016/j.phpro.2015.05.011](https://doi.org/10.1016/j.phpro.2015.05.011)
- [9] L. Li, R.Z. Li, S.Y. Zhang et al, A dynamic material discrimination algorithm for dual MV energy X-ray digital radiography. *Appl. Radiat. Isot.* **114**, 188-195 (2016). doi: [10.1016/j.apradiso.2016.05.018](https://doi.org/10.1016/j.apradiso.2016.05.018)
- [10] M. Bazalova, J.F. Carrier, L. Beaulieu et al, Dual-energy CT-based material extraction for tissue segmentation in Monte Carlo dose calculations. *Phys. Med. Biol.* **53**, 2439 (2008). doi: [10.1088/0031-9155/53/9/015](https://doi.org/10.1088/0031-9155/53/9/015)
- [11] G. Landry, P.V. Granton, B. Reniers et al, Simulation study on potential accuracy gains from dual energy CT tissue segmentation for low-energy brachytherapy Monte Carlo dose calculations. *Phys. Med. Biol.* **56**, 6257 (2011). doi: [10.1088/0031-9155/56/19/007](https://doi.org/10.1088/0031-9155/56/19/007)
- [12] W.V. Elmpt, G. Landry, M. Das et al, Dual energy CT in radiotherapy: current applications and future outlook. *Radiother. Oncol.* **119**, 137-144 (2016). doi: [10.1016/j.radonc.2016.02.026](https://doi.org/10.1016/j.radonc.2016.02.026)
- [13] M. Torikoshi, T. Tsunoo, M. Sasaki et al, Electron density measurement with dual-energy x-ray CT using synchrotron radiation. *Phys. Med. Biol.* **48**, 673 (2003). doi: [10.1088/0031-9155/48/5/308](https://doi.org/10.1088/0031-9155/48/5/308)
- [14] M. Yang, G. Virshup, J. Clayton et al, Theoretical variance analysis of single-and dual-energy computed tomography methods for calculating proton stopping power ratios of biological tissues. *Phys. Med. Biol.* **55**, 1343 (2010). doi: [10.1088/0031-9155/55/5/006](https://doi.org/10.1088/0031-9155/55/5/006)
- [15] N. Hünemohr, B. Krauss, C. Tremmel et al, Experimental verification of ion stopping power prediction from dual energy CT data in tissue surrogates. *Phys. Med. Biol.* **59**, 83 (2013). doi: [10.1088/0031-9155/59/1/83](https://doi.org/10.1088/0031-9155/59/1/83)
- [16] N. Peters, P. Wohlfahrt, C. Hofmann et al, Reduction of clinical safety margins in proton therapy enabled by the clinical implementation of dual-energy CT for direct stopping-power prediction. *Radiother. Oncol.* **166**, 71-78 (2022). doi: [10.1016/j.radonc.2021.11.002](https://doi.org/10.1016/j.radonc.2021.11.002)
- [17] C.W. Chang, Y. Gao, T.H. Wang et al, Dual-energy CT based mass density and relative stopping power estimation for proton therapy using physics-informed deep learning. *Phys. Med. Biol.* **67**, 115010 (2022). doi: [10.1088/1361-6560/ac6ebc](https://doi.org/10.1088/1361-6560/ac6ebc)
- [18] T.G. Flohr, C.H. McCollough, H. Bruder et al, First performance evaluation of a dual-source CT (DSCT) system. *Eur. Radiol.* **16**, 256-268 (2006). doi: [10.1007/s00330-005-2919-2](https://doi.org/10.1007/s00330-005-2919-2)
- [19] T.R.C. Johnson, B. Krauss, M. Sedlmair et al, Material differentiation by dual energy CT: initial experience. *Eur. Radiol.* **17**, 1510-1517 (2007). doi: [10.1007/s00330-006-0517-6](https://doi.org/10.1007/s00330-006-0517-6)
- [20] W.A. Kalender, W.H. Perman, J.R. Vetter et al, valuation of a prototype dual-energy computed tomographic apparatus. I. Phantom studies. *Med. Phys.* **13**, 334-339 (1986). doi: [10.1118/1.595958](https://doi.org/10.1118/1.595958)
- [21] D. Xu, D.A. Langan, X.Y. Wu et al, Dual energy CT via fast kVp switching spectrum estimation. *Proc. SPIE* **7258**, 1198-1207 (2009). doi: [10.1117/12.811650](https://doi.org/10.1117/12.811650)
- [22] L. Li, T. Zhao, Z.Q. Chen, First dual MeV energy X-ray CT for container inspection: design, algorithm, and preliminary experimental results. *IEEE Access* **6**, 45534-45542 (2018). doi: [10.1109/ACCESS.2018.2864800](https://doi.org/10.1109/ACCESS.2018.2864800)
- [23] G.T. Barnes, R.A. Sones, M.M. Tesic et al, Detector for dual-energy digital radiography. *Radiology* **156**, 537-540 (1985). doi: [10.1148/radiology.156.2.4011921](https://doi.org/10.1148/radiology.156.2.4011921)



- [24] B.K. Stewart, H.K. Huang, Single-exposure dual-energy computed radiography. *Med. Phys.* **17**, 866-875 (1990). doi: [10.1118/1.596479](https://doi.org/10.1118/1.596479)
- [25] M.M. Goodsitt, Beam hardening errors in post-processing dual energy quantitative computed tomography. *Med. Phys.* **22**, 1039-1047 (1995). doi: [10.1118/1.597590](https://doi.org/10.1118/1.597590)
- [26] Y.X. Xing, L. Zhang, X.H. Duan et al, A reconstruction method for dual high-energy CT with MeV X-rays. *IEEE Trans. Nucl. Sci.* **58**, 537-546 (2011). doi: [10.1109/TNS.2011.2112779](https://doi.org/10.1109/TNS.2011.2112779)
- [27] Z.J. Chi, L.X. Yan, Z. Zhang et al, Diffraction based method to reconstruct the spectrum of the Thomson scattering x-ray source. *Rev. Sci. Instrum.* **88**, 045110 (2017). doi: [10.1063/1.4981131](https://doi.org/10.1063/1.4981131)
- [28] M.J. Willemink, M. Persson, A. Pourmorteza et al, Photon-counting CT: technical principles and clinical prospects. *Radiology* **289**, 293-312 (2018). doi: [10.1148/radiol.2018172656](https://doi.org/10.1148/radiol.2018172656)
- [29] S. Leng, M. Bruesewitz, S.Z. Tao et al, Photon-counting detector CT: system design and clinical applications of an emerging technology. *Radiographics* **39**, 729-743 (2019). doi: [10.1148/rg.2019180115](https://doi.org/10.1148/rg.2019180115)
- [30] T. Flohr, M. Petersilka, A. Henning et al, Photon-counting CT review. *Phys. Med.* **79**, 126-136 (2020). doi: [10.1016/j.ejmp.2020.10.030](https://doi.org/10.1016/j.ejmp.2020.10.030)
- [31] See <https://www.aps.anl.gov/Science/Scientific-Software/XOP> for the X-ray cross section data of different materials (last accessed October 29, 2024).
- [32] H.R. Weller, M.W. Ahmed, H.Y. Gao et al, Research opportunities at the upgraded HI-γS facility. *Prog. Part. Nucl. Phys.* **62**, 257-303 (2009). doi: [10.1016/j.pnpnp.2008.07.001](https://doi.org/10.1016/j.pnpnp.2008.07.001)
- [33] S. Gales, K.A. Tanaka, D.L. Balabanski et al, The extreme light infrastructure—nuclear physics (ELI-NP) facility: new horizons in physics with 10 PW ultra-intense lasers and 20 MeV brilliant gamma beams. *Rep. Prog. Phys.* **81**, 094301 (2018). doi: [10.1088/1361-6633/aacfe8](https://doi.org/10.1088/1361-6633/aacfe8)
- [34] H.W. Wang, G.T. Fan, L.X. Liu et al, Commissioning of laser electron gamma beamline SLEGS at SSRF. *Nucl. Sci. Tech.* **33**, 87 (2022). doi: [10.1007/s41365-022-01076-0](https://doi.org/10.1007/s41365-022-01076-0)
- [35] N. Muramatsu, M. Yosoi, T. Yorita et al, SPring-8 LEPS2 beamline: A facility to produce a multi-GeV photon beam via laser Compton scattering. *Nucl. Instrum. Methods Phys. Res., Sect. A* **1033**, 166677 (2022). doi: [10.1016/j.nima.2022.166677](https://doi.org/10.1016/j.nima.2022.166677)
- [36] S. Kulpe, M. Dierolf, B. Günther et al, Spectroscopic imaging at compact inverse Compton X-ray sources. *Phys. Med.* **79**, 137-144 (2020). doi: [10.1016/j.ejmp.2020.11.015](https://doi.org/10.1016/j.ejmp.2020.11.015)
- [37] Z.J. Chi, Y.C. Du, L.X. Yan et al, K-edge imaging based on a Thomson scattering x-ray source. *Proc. SPIE* **12169**, 297-304 (2022). doi: [10.1117/12.2622201](https://doi.org/10.1117/12.2622201)
- [38] Z.J. Chi, H.Z. Zhang, J. Lin et al, Simultaneous fluorescence and Compton scattering computed tomography based on linear polarization X-ray. *Nucl. Sci. Tech.* **35**, 1–10 (2024). doi: [10.1007/s41365-024-01525-y](https://doi.org/10.1007/s41365-024-01525-y)
- [39] Z.J. Chi, Y.C. Du, L.X. Yan et al, Experimental feasibility of dual-energy computed tomography based on the Thomson scattering X-ray source. *J. Synchrotron Radiat.* **25**, 1797-1802 (2018). doi: [10.1107/S1600577518012663](https://doi.org/10.1107/S1600577518012663)
- [40] H.E. Johns, J.R. Cunningham, *The physics of radiology*, 4th edn. (Charles C. Thomas, Springfield, 1983), pp. 146-148.
- [41] Z.J. Chi, H.Z. Zhang, J.Y. Sun et al, An effective method towards large field-of-view gamma-ray computed tomography based on an inverse Compton scattering light source. *ChinaXiv*. doi: [10.12074/202412.00136](https://doi.org/10.12074/202412.00136)
- [42] S. Agostinelli, J. Allison, K.A. Amako et al., GEANT4—a simulation toolkit. *Nucl. Instrum. Methods Phys. Res., Sect. A* **506**, 250 (2003). doi: [10.1016/S0168-9002\(03\)01368-8](https://doi.org/10.1016/S0168-9002(03)01368-8)
- [43] Y.C. Du, H. Chen, H.Z. Zhang et al., A very compact inverse Compton scattering gamma-ray source. *High Power Laser and Particle Beams* **34**, 104010 (2022). doi: [10.11884/HPLPB202234.220132](https://doi.org/10.11884/HPLPB202234.220132)
- [44] Q. Gao, H. Zha, J.R. Shi et al., Design and test of an X-band constant gradient structure. *Phys. Rev. Accel. Beams* **27**, 090401 (2024). doi: [10.1103/PhysRevAccelBeams.27.090401](https://doi.org/10.1103/PhysRevAccelBeams.27.090401)
- [45] Z.J. Chi, Y.C. Du, W.H. Huang et al., Energy-angle correlation correction algorithm for monochromatic computed tomography based on Thomson scattering X-ray source. *J. Appl. Phys.* **122**, 234903 (2017). doi: [10.1063/1.4996324](https://doi.org/10.1063/1.4996324)
- [46] See <https://www.nist.gov/pml/x-ray-mass-attenuation-coefficients> for the standard data of Al, Fe, and Pb (last accessed November 7, 2024).
- [47] W. Fang, L. Li, Attenuation image referenced (AIR) effective atom number image calculation for MeV dual-energy container CT using image-domain deep learning framework. *Results Phys.* **35**, 105406 (2022). doi: [10.1016/j.rinp.2022.105406](https://doi.org/10.1016/j.rinp.2022.105406)
- [48] V.P. Singh, N.M. Badiger, Effective atomic numbers of some tissue substitutes by different methods: A comparative study. *J. Med. Phys.* **39**, 24–31 (2014). doi: [10.4103/0971-6203.125489](https://doi.org/10.4103/0971-6203.125489)
- [49] M. Kurudirek, M. Büyükyıldız, Y. Özdemir, Effective atomic number study of various alloys for total photon interaction in the energy region of 1 keV–100 GeV. *Nucl. Instrum. Methods Phys. Res., Sect. A* **613**, 251–256 (2010). doi: [10.1016/j.nima.2009.11.061](https://doi.org/10.1016/j.nima.2009.11.061)
- [50] M.M. Hosamani, N.M. Badiger, Determination of effective atomic number of composite materials using backscattered gamma photons—a novel method. *Chem. Phys. Lett.* **695**, 94–98 (2018). doi: [10.1016/j.cplett.2018.02.012](https://doi.org/10.1016/j.cplett.2018.02.012)
- [51] M. Kurudirek, Effective atomic number of soft tissue, water and air for interaction of various hadrons, leptons and isotopes of hydrogen. *Int. J. Radiat. Biol.* **93**, 1299–1305 (2017). doi: [10.1080/09553002.2018.1388546](https://doi.org/10.1080/09553002.2018.1388546)